

**Decomposition of silicon carbide at high pressures and temperatures**

Kierstin Daviau\* and Kanani K. M. Lee

*Department of Geology & Geophysics, Yale University, New Haven, Connecticut 06511, USA*

(Received 13 June 2017; revised manuscript received 14 August 2017; published 3 November 2017)

We measure the onset of decomposition of silicon carbide, SiC, to silicon and carbon (e.g., diamond) at high pressures and high temperatures in a laser-heated diamond-anvil cell. We identify decomposition through x-ray diffraction and multiwavelength imaging radiometry coupled with electron microscopy analyses on quenched samples. We find that B3 SiC (also known as 3C or zinc blende SiC) decomposes at high pressures and high temperatures, following a phase boundary with a negative slope. The high-pressure decomposition temperatures measured are considerably lower than those at ambient, with our measurements indicating that SiC begins to decompose at  $\sim 2000$  K at 60 GPa as compared to  $\sim 2800$  K at ambient pressure. Once B3 SiC transitions to the high-pressure B1 (rocksalt) structure, we no longer observe decomposition, despite heating to temperatures in excess of  $\sim 3200$  K. The temperature of decomposition and the nature of the decomposition phase boundary appear to be strongly influenced by the pressure-induced phase transitions to higher-density structures in SiC, silicon, and carbon. The decomposition of SiC at high pressure and temperature has implications for the stability of naturally forming moissanite on Earth and in carbon-rich exoplanets.

DOI: [10.1103/PhysRevB.96.174102](https://doi.org/10.1103/PhysRevB.96.174102)**I. INTRODUCTION**

Silicon carbide (SiC) attracts wide interest owing to its semiconductor nature, high bulk modulus, and high melting temperature [1]. Naturally occurring SiC forms under very reducing conditions and is rare on Earth, found in small quantities in numerous geologic settings [2]. SiC is also abundant in the spectrum of carbon stars [3] and is found to be present in meteorites [4]. The discovery of extrasolar planets [5] and the possibility of carbon-rich solar systems largely composed of SiC [6,7] has expanded the areas in which we expect to find naturally occurring SiC, increasing the need for high-pressure and -temperature studies.

A large body of work has been performed to better understand aspects of the SiC phase diagram at various pressure and temperature conditions [8–21]. The ambient-pressure, high-temperature behavior of the Si-C system has been explored in detail [11]. Ambient temperature studies have explored a wide range of pressure conditions. Zhuravlev *et al.* [20] proposed the use of SiC as a pressure standard in the diamond-anvil cell (DAC) based on elasticity studies carried out up to 80 GPa. It was found that cubic B3 SiC transforms to the B1 structure at a pressure of  $\sim 100$  GPa when compressed in a DAC at room temperature [19]. This transition was additionally observed in shock studies [13,15] and was recently reported at lower pressures of  $\sim 60$  GPa when heated in a laser-heated DAC [10]. Additional studies of the high-pressure and -temperature (high P-T) behavior of SiC include measurements of the thermal equation of state (EOS) up to pressures of 8.1 GPa and temperatures of 1100 K [18] as well as the thermal expansion of SiC up to pressures of 80 GPa and temperatures of 1900 K [21].

Upon investigating the simultaneous high P-T behavior of SiC [10], we also found that SiC decomposes to its elemental constituents, silicon and carbon. This study focuses on the decomposition at high pressures and simultaneous high tem-

peratures. At ambient pressures, it has been seen that SiC melts incongruently with the Si fraction coming out as a liquid and the C fraction remaining as a solid [11]. The ambient pressure decomposition of SiC into solid C plus liquid Si begins at  $\sim 2840$  K in experiments [11] while it is predicted to occur at higher temperatures of 3100 K in computations [22,23]. Previous explorations of high-pressure melting and possible decomposition have gone up to  $\sim 10$  GPa while heating to temperatures as high as 3500 K [8,9,12,14,16,17]. Confusion has arisen as to whether or not decomposition continues upon increasing pressure as well as to the nature of the slope (positive or negative) of the phase boundary of the reaction. For instance, one study finds that SiC melts incongruently (decomposition to C solid and Si liquid) along a positively sloped phase boundary [17]. Based on the increase in the solubility of C in liquid Si with increasing pressure, they predict that decomposition does not continue past about  $\sim 10$  GPa, after which SiC melts congruently. In nearly the same pressure and temperature range, another group [16] reports contradictory results, finding that SiC does not decompose at pressure and that congruent melting follows a negative phase boundary.

Using the laser-heated DAC in conjunction with a variety of *in situ* and *ex situ* quenched analysis techniques, we explore the decomposition behavior of SiC at pressures up to  $\sim 80$  GPa and temperatures up to  $\sim 3200$  K. Using x-ray diffraction (XRD), multiwavelength imaging radiometry [24], Raman spectroscopy, focused ion beam (FIB) cross sections, and electron microscopy we investigate SiC decomposition at pressures between  $\sim 10$  and 80 GPa. We find that B3 SiC decomposes at pressure following a negative phase boundary. However, we do not observe decomposition in SiC after it transitions to the B1 structure even upon heating to a maximum temperature of  $\sim 3200$  K at 81 GPa.

**II. METHODS**

Our samples consist of a fine-grained powder of cubic B3 SiC from Alfa Aesar ( $\beta$ -SiC product no. 14165, lot no. I21  $\times$  047), confirmed by XRD. We often observed additional weak

\*kierstin.daviau@yale.edu

TABLE I. Upstream (downstream) temperatures listed for first evidence of diamond formation as revealed by XRD. Uncertainties in temperatures are reported as the difference between the up and downstream sides or as the difference in temperature between the last pattern without diamond diffraction and the first pattern with diamond diffraction. The reported uncertainty is the larger of the two (Fig. 6). \*Pressure determined by Ne [20,28].

Sample Name	Preheat Pressure (GPa)	Pressure at diamond formation* (GPa)	Temperature at diamond formation (K)	Diamond $hkl$	Diamond position [ $d$ -spacing (Å)]	Calculated position <sup>a</sup> [ $d$ -spacing (Å)]
XRD_001	9.7	10.1	2327	111	2.053 (high $T$ ) <sup>b</sup>	2.044
XRD_002	17.5	20.7	2160 (2223)	111 220	2.024 1.242	2.028 1.242
XRD_003	30.0	32.4	2074 (2260)	111	2.011	2.012
XRD_004	54.1	51.5	1926 (1964)	111	1.993	1.987

<sup>a</sup>Reference [64].

<sup>b</sup>At pressures of  $\sim 10$  GPa the Ne 111 reflection overlaps closely with the C diamond 111 reflection. Because of this we use the C diamond 111 reflection collected at high  $T$ , after Ne has melted.

reflections from the 101 and 103  $hkl$  lines of 6H SiC in our starting diffraction patterns. Based on the relative intensities, however, the abundance of the 6H SiC ( $\alpha$ -SiC) phase is likely less than 3%. Scanning electron microscope (SEM) images confirmed that the starting grain size varied between  $\sim 0.1$  and  $1 \mu\text{m}$ . For laser heating experiments, the powder was compressed in an 80–120- $\mu\text{m}$  hole drilled in the center of a preindented Re gasket using the stepped anvil technique [25]. Both 200- and 300- $\mu\text{m}$  culet diamonds were used. Several different materials were used as a pressure medium and thermal insulation including NaCl, KCl, KBr, Ar, Ne, SiO<sub>2</sub>, and self-insulation (no medium). Care was taken to dry out the samples by placing the completed samples into an oven at  $\sim 350$  K overnight. Samples heated evenly and steadily with all materials except NaCl, where sample temperatures tended to run away, suggesting a change in the absorption character of NaCl at high temperatures, although no obvious color change was observed [26]. KCl, KBr, Ne, and self-insulation were ultimately preferred to ensure steady heating and minimize contamination or oxidation of the SiC sample.

Pressure was measured using the Raman shift of the diamond edge [27] or, when available, the room-temperature equation of state (EOS) of Ne [28] with corrections provided by [20]. The Raman system used is a Horiba-Jobin Yvon HR-800 Raman microscope equipped with a 50-mW green laser (532 nm) with an 1800 lines/mm grating (Table SI in the Supplemental Material [29]). After heating, sample pressures typically increased by 10%–20% in the heated region, although

the largest pressure change observed was an increase by 50%. A couple of high-pressure samples dropped in pressure after heating (Tables I and II). Our laser heating experiments were done in two locations: (1) at the HPCAT-IDB beamline at the Advanced Photon Source (APS) in which we used XRD to probe crystal structure and phase changes *in situ* [30] and (2) at Yale University where we used the multiwavelength imaging radiometry temperature measurement system to map temperatures and emissivities to explore temperature gradients and corresponding optical changes in SiC [24]. A combination of the findings from the two different kinds of experiments and *ex situ* analysis methods were used to constrain the onset of SiC decomposition at high P-T.

Irrespective of the heating location, pressure medium, or starting pressure of the sample, the same procedure was followed in each heating experiment. Samples were heated systematically in the center of the sample chamber by gradually increasing laser power, remaining for several seconds to a minute at each power, and taking regularly spaced temperature measurements to track the sample's response. For samples heated at HPCAT-IDB, diffraction patterns were also taken throughout the heating. After each heating round, the sample was temperature quenched and either a diffraction pattern (at HPCAT-IDB) or a white light image (at Yale University) was taken to characterize changes in the quenched sample as a result of the previous heating. Each sample was heated to a peak temperature between 1500 and 3200 K in this manner, aiming to increase the temperature by  $\sim 100$  K increments. We

TABLE II. Samples heated on one side and measured by multiwavelength imaging radiometry. Uncertainties in the temperature are no more than  $\pm 8\%$ , unless listed [24]. \*Pressure determined by the Raman shift of the diamond anvil [27].

Sample Name	Preheat Pressure* (GPa)	Postheat Pressure* (GPa)	Insulation media	Temperature of dark absorbing feature (K)
4CLR_001	16	24	Self-insulation	2060
4CLR_002	31	33	KCl	2180
4CLR_003	39	39	Ne	2220
4CLR_004	42	48	Self-insulation	2100
4CLR_005	63	61	Self-insulation	2000
4CLR_006	81	73 (3200 K) 79 (1200 K)	KBr	3200 (no CDC observed) 1200 (CDC observed)

ramp-heated several samples [31] in order to account for diffusive effects brought about by the gradual temperature increase and long heating duration. We saw the same optical features and changes in both the gradually heated (over minutes) and ramp-heated (over seconds) samples using the multiwavelength imaging radiometric temperature mapping technique.

Temperature was determined by measuring and fitting the thermal emission from the sample as described in Ref. [30] for those heated at HPCAT-IDB and in Ref. [24] for those heated at Yale. Wavelength-dependent absorption in laser-heated DAC samples has recently been identified as a potentially large source of error in spectroscopic temperature measurements [32]. In order to correct for this effect in our samples, we measured the absorption spectra of SiC at the offline VIS/IR lab at the National Synchrotron Light Source II (NSLS II) at Brookhaven National Lab (BNL) (Figure S1, [29]). Absorption measurements over visible wavelengths were taken for both heated and unheated SiC at three different pressures (13, 35, and 52 GPa) in order to account for possible pressure effects in the absorption (Figure S2, [29]). Based on these measurements and the forward modeling outlined in Ref. [32], we find that our measured temperatures differ by only  $\sim 50$  K from their predicted actual sample temperatures (Fig. S3, S4 [29]). Since the wavelength range used to calculate the temperature at the HPCAT-IDB heating system is a subset of the wavelength range used at Yale ( $\sim 600$ – $800$  nm versus  $580$ – $905$  nm), our temperature correction model can be applied to measurements taken at both locations. As our temperature error bars typically stretch to  $\pm 8\%$  of the measured temperature [24], we do not additionally correct the measured temperatures for absorption effects. Details of the absorption measurements and of the temperature correction forward modeling can also be found in the Supplemental Material [29].

Temperature-quenched samples were further investigated by Raman spectroscopy at ambient and high pressures. Additionally, quenched samples were cross sectioned using FIB and analyzed by SEM for texture, energy dispersive spectroscopy (EDS) for qualitative composition, electron backscatter diffraction (EBSD) for crystal structure, and electron probe microanalysis (EPMA) and wavelength dispersive spectroscopy (WDS) to determine quantitative composition. Further details of the analysis equipment can be found in Table SI of the Supplemental Material [29].

### III. RESULTS

The two kinds of experiments allowed us to probe different *in situ* properties during heating. Measurements completed at the synchrotron determined structural changes through the use of XRD, while the measurements performed on the multiwavelength imaging radiometry system determined optical changes and apparent temperature gradients across the hot sample through two-dimensional temperature mapping. We first present the structural results from diffraction, and then present the optical results.

#### A. X-ray diffraction

While heating SiC, we observe the emergence of new diffraction peaks corresponding to cubic diamond [Fig. 1(a)]. The temperature and pressure of the diamond appearance, as well as the  $d$ -spacing of the diamond peaks from quenched

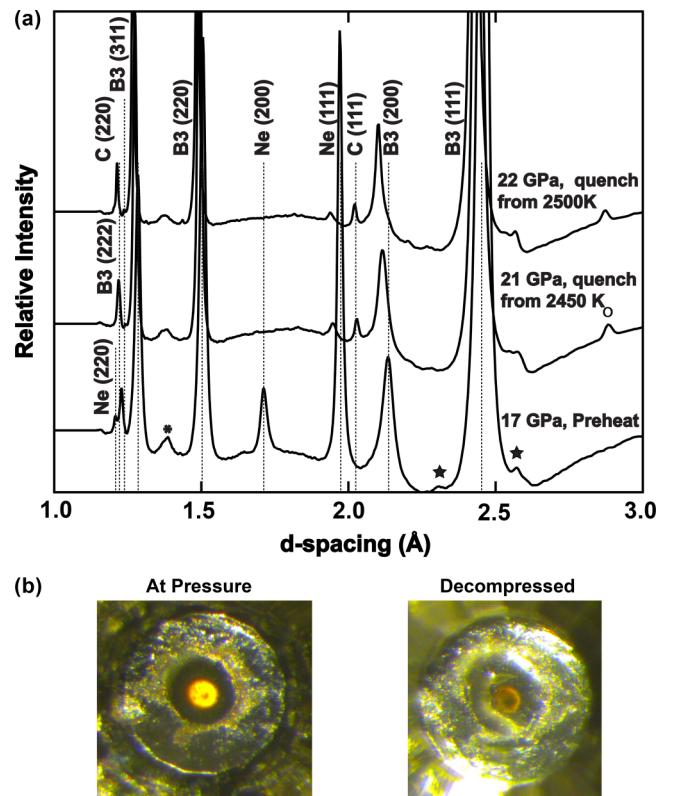


FIG. 1. (a) Diffraction patterns of temperature-quenched samples from before, during and after double-sided laser heating B3 SiC at  $\sim 20$  GPa (XRD\_002). The  $hkl$  reflections of B3 SiC and Ne are labeled, as well as those from C diamond that appear after heating to high temperatures. In this case diamond appeared at upstream (downstream) temperatures of 2160 K (2333 K), but the temperature was increased to over 2400 K before taking a temperature-quenched pattern. Reflections from the Re gasket are labeled with an asterisk, reflections from 6H-SiC are labeled with a star, and an unidentified peak appearing at high temperature is labeled with an empty circle. (b) Optical images of the same sample taken after heating. The left image is of the sample under pressures at  $\sim 22$  GPa while the right image is after decompression. There are three different regions of the sample: (1) gray, unheated material on the outer edge of the sample chamber, (2) translucent material surrounding the hottest region, and (3) a black, opaque center where the laser was focused and temperatures, presumably, the hottest. We do not observe evidence for diamond-anvil damage upon unloading the sample.

patterns as compared to the calculated  $d$ -spacing, are listed in Table I. We take the formation of diamond in our SiC samples to indicate the onset of decomposition. Once formed, the diamond reflections remain even while heating to temperatures below the initial decomposition temperature. The diamond peaks also remain upon quench and decompression, indicating that the decomposition is irreversible on the time scales of our experiments. Due to our inability to reverse the experiments we are limited to only measuring the first onset of decomposition. Temperature gradients across the sample prevent us from determining the extent of decomposition as well. Due to the amount of cold material through which the x-rays pass, the B3 SiC reflections never disappear and remain in samples even after decompression has begun (see the Supplemental Material [29]).

We do not see the appearance of Si diffraction in any of our heating runs. There are several possibilities as to why this may be the case. At the high temperatures of SiC decomposition, Si is likely a liquid. The melting temperature of Si was experimentally measured to be low, around 1000 K, while at pressures up to  $\sim 15$  GPa [33–35]. If the Si melting point remains low at increased pressures then we would not expect to see Si diffraction at high temperatures. Upon quenching the laser at high pressure, Si may cool to an amorphous state [36], and therefore diffraction would not be observed. Impurities also play an important role in the structure of Si upon pressure unloading. It has been observed that Si quenches to an amorphous structure when unloaded in the presence of impurities [37]. If C is acting as the impurity in our system, it may prevent Si from crystallizing under pressure. This would result in Si being absent from both temperature-quenched and pressure-quenched XRD patterns.

The findings from the XRD measurements are supported by FIB'ed cross sections of heated samples. Samples were cross sectioned by first removing the excess gasket material by electrical discharge machining (EDM) and then FIB'ed using a FEI Helios NanoLab DualBeam system with gallium ions ( $\text{Ga}^+$ ) to etch away the unheated sample and reach the heated region [31]. We do not observe any adverse effects on the sample cross section from the FIB process, as we polish the cross section with a very low ion current before doing any SEM or compositional analysis. We also check for any lingering Ga contamination in the sample and consistently find that the polished region of interest is free of Ga. Ga can collect in voids or cracks along the sample surface but remains localized and visible [38]. Once the hot spot was exposed and polished, we imaged the area with electron microscopy and determined composition using EDS or WDS and EBSD analysis techniques [29]. Figure 2 displays the map view of 4CLR\_003, a sample heated at 39 GPa, as well as the backscattering electron (BSE) image of the cross section and the C and Si abundance WDS maps collected by EPMA. The dark grains in the BSE image correspond to regions of C enrichment and Si depletion, while the center of the heated area is slightly depleted in C and enriched in Si. We do not see any large, isolated grains of Si, consistent with Si forming small amorphous grains that remain invisible to x-rays. As we heat in one location throughout the experiment with a laser spot size of  $\sim 20$ – $30$   $\mu\text{m}$ , we only expect to see evidence of decomposition across a similarly sized region.

EBSD measurements were completed on a large carbon grain of  $\sim 4$   $\mu\text{m}$  found in cross section, confirming that the structure of the grain is cubic diamond (see Supplemental Material, Fig. S5 [29]). We see considerable grain growth across the heated portion of this sample, and find that decomposition features are present across  $\sim 40$   $\mu\text{m}$  of the sample. Small diamond grains are found both on the interior and exterior of the SiC grains that began decomposition. The presence of Si, C, and SiC grains after decomposition may contribute to the pressure increase observed after heating.

### B. Multiwavelength imaging radiometry

Using the multiwavelength imaging radiometric temperature mapping system at Yale University we investigate

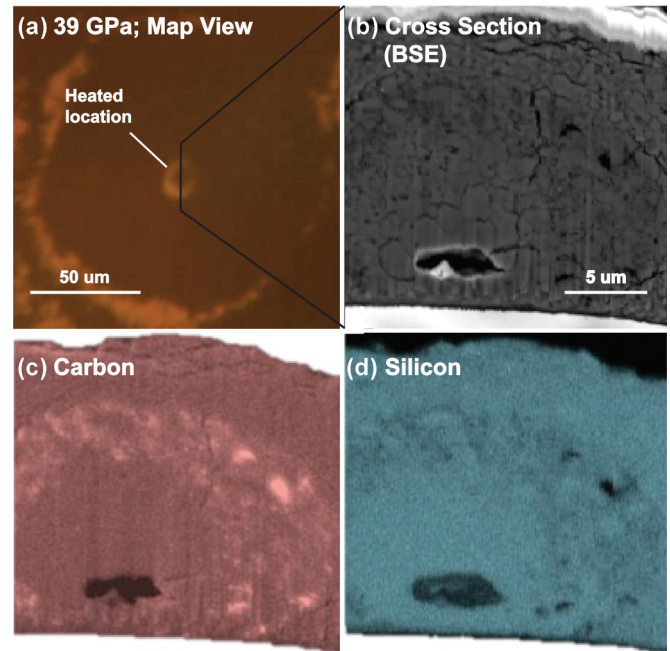


FIG. 2. (a) Photomicrograph of 4CLR\_003, heated at 39 GPa, displaying characteristic optical changes across the heated location using both transmitted and reflected light. (b) BSE image of the corresponding FIB'ed cross section across the hot spot. Compositional map of sample cross sections measured by EPMA EDS of (c) C and (d) Si. Brighter areas denote higher relative abundance, while darker areas denote lower relative abundance. We observe concentrated C-rich and Si-poor grains as well as a larger central region with slight Si enrichments.

the optical changes that SiC undergoes at high P-T [24]. The most dramatic change that we observe is a change in the sample's absorbance with increasing temperature. This absorbance change can be seen clearly in both the emissivity (light intensity from thermal emission) and the temperature measurements from our system. Changes in sample emissivity have been used previously as a diagnostic for phase changes [39,40] as emissivity is a material property.

Our starting powder is semiopaque when loaded and remains so after compression, even at the highest pressures attained in these experiments. Transmitted light measurements on our laser heating system record only a very dim passage of white light through the starting material. After heating to low temperatures ( $\sim 1000$  K) the SiC begins to lose its opacity and becomes more transparent to white light. The transmitted light images collected by a charge-coupled device (CCD) camera show a transparent disk covering the area of the sample that has been heated. At higher temperatures samples develop dark, absorbing spots in the heating location. These appear as absorbing features in the middle of the transparent disk [Figs. 1(b) and 3(e)].

We can see evidence of these absorbing features in the temperature and emissivity maps collected during heating (Fig. 3). At low temperatures, below decomposition of SiC, the temperature and emissivity maps show similar symmetric profiles: highest values at the center with decreasing values radially outward. Samples heated to high enough temperatures

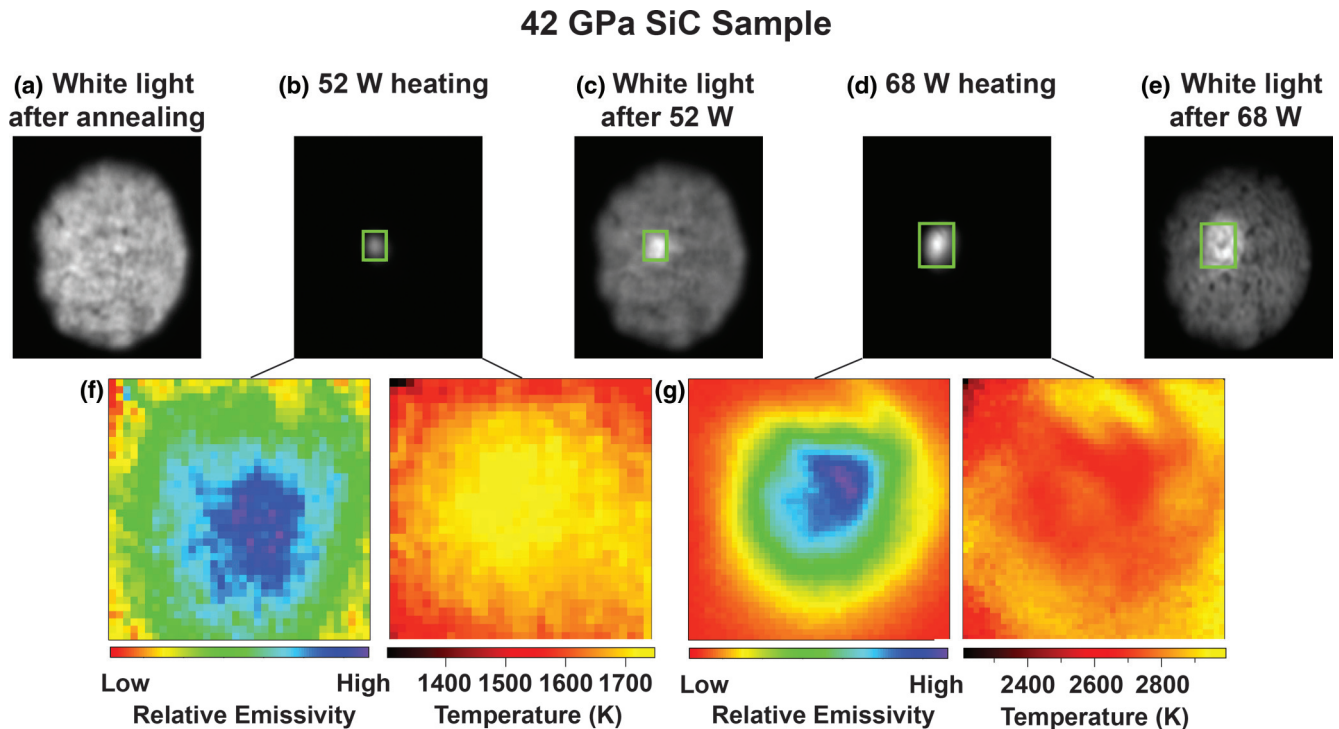


FIG. 3. Progression of the absorption changes observed in a 42-GPa sample laser heated with temperatures measured by multiwavelength imaging radiometry [24]. The top row of images is of the sample in the 640-nm wavelength captured by the CCD camera during the heating experiment. The bottom row contains the corresponding emissivity and temperature maps found by fitting three additional wavelength images (580, 766, 905 nm). Top row from left to right: (a) transmitted white light through the sample after initial annealing at low temperatures; (b) *in situ* thermal emission from midway through heating (52 W of laser power); (c) white light image after 52 W heating (note enhanced transparency as compared to surrounding areas); (d) *in situ* thermal emission of final heating at 68 W; (e) white light after final 68 W heating. Bottom row from left to right: (f) *in situ* emissivity and temperature map from the 52 W heating; (g) *in situ* emissivity and temperature map from the 68 W heating. Notice that the sample becomes significantly more transparent over the heated region (green outline) and that a darker region becomes apparent in the white light image after the final heating. The emissivity and temperature maps match up well during the early heating but become uncorrelated later in the heating run. Green outlines correspond to the region of the image where temperature and emissivity are mapped.

to become absorbing continue to show symmetric emissivity maps; however, temperature maps no longer record the highest apparent temperatures at their centers, suggesting wavelength dependency of the absorption [Figs. 3(f) and 3(g)]. The apparent temperature maps instead indicate that the center is *cooler* than the edges and have a reverse profile with increasing temperature around the *edge* of the heating area. We report the temperature surrounding the apparent cooler region. In order to explain the apparent temperature decrease, we forward-model the temperatures [32] using the measured absorption profiles and estimates of the cross-sectional layer thicknesses. This mismatch between the temperature and emissivity maps is due to the highly absorbing and wavelength-dependent characteristics of the heated area. The dark feature blocks out a portion of the thermal emission in a wavelength-dependent fashion, meaning that even though the center of the laser spot gives the most counts, it does not fit a blackbody corresponding to the highest temperature. The difference appears to be small, however, with temperature aliasing typically less than 100 K across the heated area ( $\sim 20 \mu\text{m}$ ) (Figs. S3, S4). See the Supplemental Material [29] for a detailed discussion of the temperature correction forward model.

Table II lists the pressure and temperature conditions at which samples first displayed characteristics of the highly

absorbing feature. The feature was identified by the mismatch between the emissivity and temperature maps and confirmed by postheat white light images when available (Fig. 3). Our interpretation of these features is further informed by the appearance of carbide-derived carbon (CDC) signals in the Raman spectra [41] (Fig. 4; see the Supplemental Material [29]) as well as the features observed in FIB'ed cross sections. The initial shift to optical transparency may be due to the annealing of dislocations and reorganization of grain boundaries, as the transparency of SiC has previously been correlated with grain orientation and internal microstructure [42]. We do not see structural changes in SiC at low temperatures in the XRD, and the lower-temperature regions of cross sections are featureless aside from considerable grain growth as compared to the starting material.

The sudden increase in absorption appears to be related to decomposition based on the strong correlation between the P-T conditions at which we see diamond XRD peaks emerge and the conditions at which the strongly absorbing features appear. We use the change in the temperature maps as evidence for the absorbing feature and, therefore, SiC decomposition. Similar to the diamond XRD peaks, once the heated SiC forms an opaque region at high temperature it does not revert back to being more transparent at lower temperatures or upon

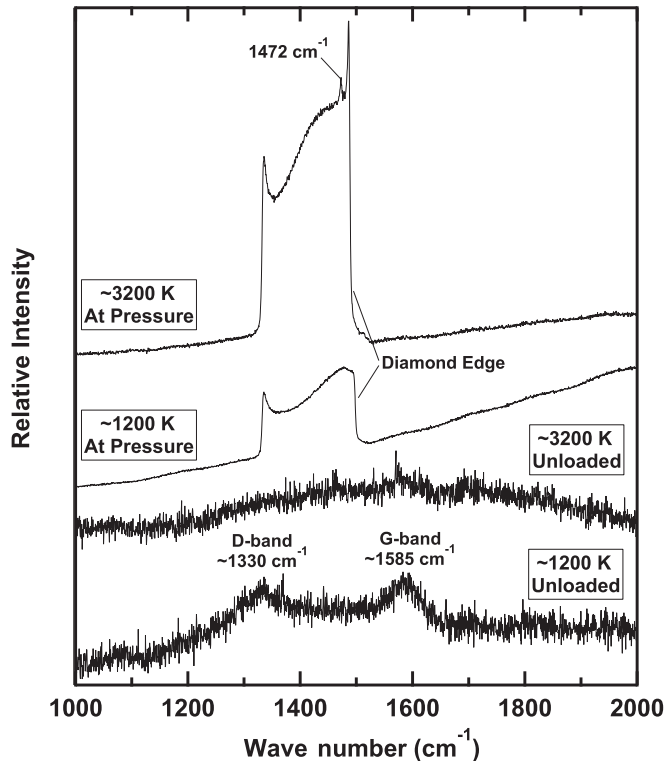


FIG. 4. Raman spectra from 4CLR\_006 after heating at 81 GPa using the multiwavelength imaging radiometric temperature mapping system. The top two patterns are of the compressed sample while the bottom two patterns are of the same sample after unloading from the diamond cell. We see a small additional peak at  $\sim 1470 \text{ cm}^{-1}$  in the center of the heated area while at pressure that is absent from the surrounding region as well as from the unloaded pattern. After unloading we see no evidence of decomposition throughout the hottest region but do see the characteristic *D* and *G* band signals of CDC in the surrounding, annealed area. The lack of decomposition in the hot spot is supported by *in situ* measurements, as throughout the entire heating and up to the highest temperatures of  $\sim 3200 \text{ K}$ , the temperature and emissivity maps continue to display symmetric behavior across the hot spot.

decompression. As both the phases of carbon (graphite and diamond, depending on pressure [43]) and the phases of silicon (I, II, V, depending on pressure [44,45]) have very different optical properties from one another and from SiC, it is not surprising that the breakdown of SiC to C and Si will result in visible changes across the heated area. It is possible that the absorbing feature is due to the presence of elemental Si forming upon decomposition.

#### IV. DISCUSSION

We make several unexpected observations in our decomposition measurements. The first observation is that the onset of decomposition at 10 GPa occurs at  $\sim 2300 \pm 200 \text{ K}$ . The closest study finding decomposition of SiC in previous work is at 3400 K at 9 GPa [17]. If both the previous data point and our data point are reliable, then this requires a steep drop in the decomposition temperature of over 1000 K across a pressure range of only 1 GPa. At pressures above 10 GPa

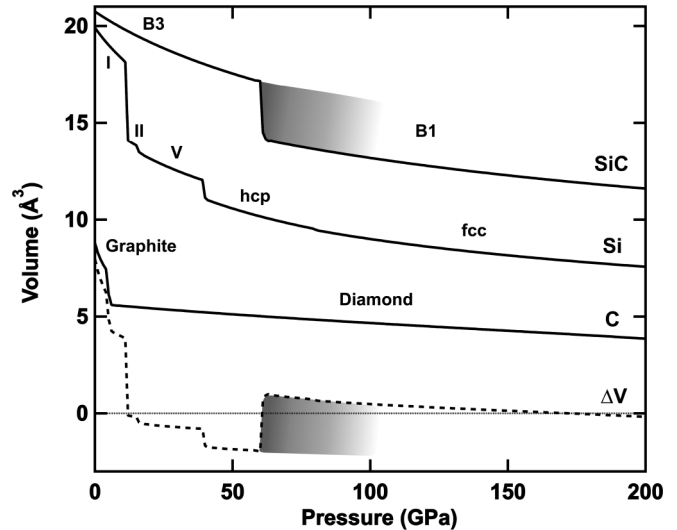


FIG. 5. The room-temperature equations of state for SiC [20,63], Si [44], and C [43,64] including high-pressure phase transitions (solid curves) as well as the curve for across the SiC to Si+C decomposition reaction (dashed curve). The  $\Delta V$  for decomposition is large and positive at low pressures ( $< \sim 12 \text{ GPa}$ ) but decreases to negative values upon the transition of Si I to Si II. The  $\Delta V$  remains negative until B3 SiC transitions to the higher-density B1 structure. At equilibrium, this reaction occurs at  $\sim 58 \text{ GPa}$  (i.e., [63]) but is kinetically hindered experimentally and is not seen before 100 GPa at room temperature [19]. The shaded region of the SiC and  $\Delta V$  curve represents the region across which the SiC volume, and therefore the  $\Delta V$  at decomposition, is dependent on the experimental conditions.

we do see a drop in the decomposition temperature with increasing pressure but following a much shallower transition boundary. In the previous study, the temperatures reported are calculated by correcting the amount of inserted energy for heat loss and then converting to temperature using the temperature dependence of the enthalpy of SiC from the National Institute of Standards and Technology Joint Army Navy and Air Force (NIST-JANAF) thermochemical tables [46]. It is also possible that their measurements may not be for the onset of decomposition, but rather well into decomposition [17].

We find a second unexpected aspect of SiC decomposition at higher pressure. At 81 GPa, SiC did not heat smoothly as observed at lower pressures. The sample instead showed only a slight glow when heating, indicating that temperatures were low; however, the sample quickly became more absorbing and the temperatures rapidly rose, but did not run away. We see no evidence of decomposition in the Raman spectra across the hottest region of that sample, which was heated to over 3200 K (Fig. 4). However, in the surrounding SiC that was annealed to very low temperatures ( $\sim 1200 \text{ K}$ ) without any sudden coupling we see the *D* and *G* band signatures of CDC in the Raman spectra taken after decompression (Fig. 4).

We explain these two unexpected features by considering the phase changes of SiC, Si, and C at high pressures. If we consider the phase diagrams and room-temperature equations of state for all three materials, we see that our unexpected observations fall at pressure conditions near where a phase change has been observed in at least one of the three components in the system. In Fig. 5 we plot the compression

curves for SiC, Si, and C, as well as the corresponding volume changes across the  $\text{SiC} \rightarrow \text{Si} + \text{C}$  decomposition reaction. Positive values of  $\Delta V$  mean that Si + C has a larger volume per (Si, C) atom pair than SiC, while negative values of  $\Delta V$  mean that SiC has the larger volume. At low pressures, when Si and C are both in their lowest-pressure structures, the volume change across the decomposition reaction is large and positive. This is consistent with low-pressure measurements finding a high decomposition temperature and positive Clapeyron slope [17]. At slightly higher pressures, however, both C and Si transition to higher-density structures, with the largest compaction occurring in the Si structure going from the diamond (Si I) to  $\beta$ -Sn (Si II) structure ( $\sim 12$  GPa at room temperature) [45]. Because of this sudden increase in Si density, the volume change across the decomposition of SiC drops to negative values. While SiC remains in its low-pressure B3 structure but Si transitions to several high-pressure, higher-density structures, the volume change across the decomposition reaction remains negative and increases in magnitude. The abrupt change in  $\Delta V$  at the transition from Si I to Si II may explain why we see such a large drop in decomposition temperature at pressures of  $\sim 10$  GPa as compared to ambient- and lower-pressure measurements. The negative  $\Delta V$  at higher pressures is consistent with the negative slope of the phase boundary that we observe for the reaction up to  $\sim 62$  GPa.

Above 60 GPa, SiC transitions from the B3 to the B1 structure at equilibrium. This transition is known to be sluggish [10], however, and is not observed until  $\sim 100$  GPa at room temperature [19]. Recent work finds that the addition of temperatures near 1700 K lowers the transition pressure closer to that expected from computations [10]. The B3 to B1 transition is accompanied by a nearly 20% decrease in volume, which is enough to switch the sign of  $\Delta V$  across the decomposition reaction back to positive values. Our measurements at 81 GPa can be explained if they are straddling the B3 to B1 transition in SiC. At these pressures and temperatures the hottest region of the sample is likely in the B1 structure [10]. We see an additional peak at  $\sim 1470 \text{ cm}^{-1}$  in the Raman spectra of the hottest region that is not found in the surrounding annealed SiC or upon quench (Fig. 4). In the B1 structure it appears to take very high temperatures to achieve decomposition, at least over 3200 K at  $\sim 80$  GPa if decomposition occurs at all. B1 SiC may decompose at higher temperatures than those explored here, perhaps following a positive Clapeyron slope as indicated by the volume change across the decomposition reaction. Based on the differences in volume, at pressures greater than  $\sim 170$  GPa, decomposition may require lower temperatures and follow a negative phase boundary once again (Fig. 5). The surrounding portion of the sample that was annealed at low temperatures ( $< \sim 1200$  K) did not reach a high enough temperature to transition to the B1 structure but did reach high enough temperatures to decompose the metastable B3 SiC. Decomposition in metastable B3 SiC would still have a large negative  $\Delta V$  across the transition and so, based on our data at lower pressures, would decompose at a low annealing temperature.

We present a phase diagram for the decomposition of SiC at high pressures and temperatures based on our experimental work as well as that reported by previous studies (Fig. 6) [11,16,17]. The shape of the decomposition boundary appears

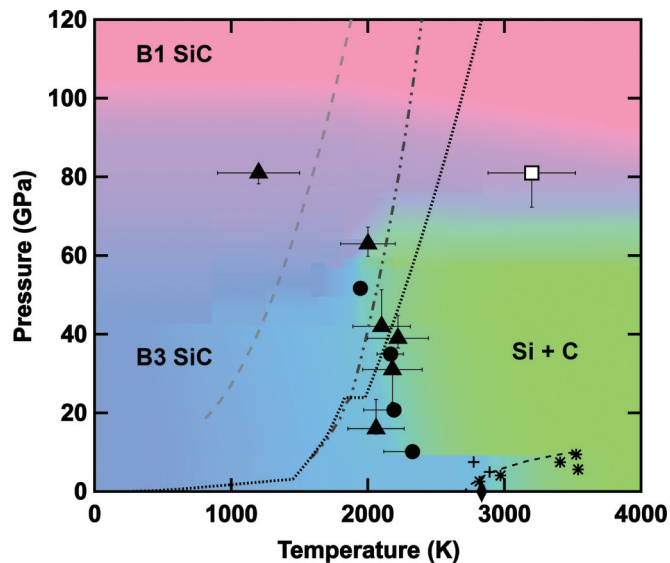


FIG. 6. Phase diagram for the high-pressure decomposition of SiC. Conditions at which the first sign of diamond diffraction appears are represented by solid circles, conditions at which absorption changes are observed by multiwavelength imaging radiometry are represented by solid triangles, and the conditions at which B1 SiC shows no evidence of decomposition is represented by an open square. Temperature error bars are as described in Tables I and II. Pressure error bars for the diffraction data are from errors in the Ne volume and are smaller than the symbols [20,28]. Pressure error bars for the multiwavelength imaging radiometric measurements are from the spread in pressure across the sample chamber before and after heating as determined by the Raman edge of diamond [27]. Previous data observing decomposition are represented by solid diamonds [11] and by asterisks for the previously reported extrapolated phase boundary [17]. Previous data that did not observe decomposition are represented by plus signs [16]. We show the regions of phase stability through colored shading with blue corresponding to B3 SiC, green to Si+C, pink to B1 SiC, and the mixed purple region representing the area where the B3 to B1 transition is kinetically hindered. Temperature profiles for Earth's mantle (dash-dot [54], dotted [55]) as well as for a subducting slab (dashed [56]) are plotted. Both mantle geotherms cross the decomposition boundary for SiC, indicating that moissanite has a region of instability within the mantle.

to be strongly influenced by the structural transitions in the Si, C, and SiC components. As we did not measure decomposition in the B1 structure, we do not include a decomposition boundary for B1 SiC, although it may decompose at higher temperatures than those explored here. At the temperatures of decomposition Si is likely a liquid [33–35], and thus the decomposition of B3 SiC is an example of incongruent melting. It is possible that B1 SiC is stable to high enough temperatures to melt congruently and so does not undergo decomposition. We note that below 60 GPa, high-temperature B3 SiC does not favor a transition to B1 SiC over decomposition due to a Clapeyron slope near zero for the B3 to B1 transition at equilibrium conditions [10].

In this way we are able to join our high-pressure results with those conducted at lower pressures [16,17], resolving some of the confusion and inconsistencies with the previous studies. We are still unsure, however, why the authors of [16] observed

melting of SiC but not decomposition at pressures of 5 and 7.5 GPa. It is possible that the SiC in their experiments was still below the decomposition temperature since we expect the Clapeyron slope to be positive in this pressure regime, although we would not expect to see any melting if this is the case. What is interesting about this region is that it is above the transition pressure of C graphite to C diamond but below the transition of Si I to Si II. It is possible that the decomposition reaction behaves differently in this window where diamond is stable but the  $\Delta V$  across the transition is still positive. As an alternative explanation for the lack of observations of diamond formation in Ref. [16], we suggest that the small grain size may have made diamond difficult to detect in quenched diffraction analyses. We find that our diamond grains are very small, on the order of several  $\mu\text{m}$  at most, and quite localized. Moving even 5  $\mu\text{m}$  away from the heating location causes the diamond diffraction to disappear in most of our experiments. It would be difficult to locate a diamond grain in a postheated sample that had been formed away from a synchrotron x-ray diffraction beam line, making it challenging to determine with certainty that a sample did not decompose.

Kinetic effects may also contribute to differences between the previous and current studies. The B3 to B1 transition in SiC is kinetically hindered [10] as are transitions in other carbon materials (e.g., [47,48]). We find here that decomposition of SiC is also kinetically slow, meaning that grain size may play a role in the extent of decomposition observed. Our starting grain size ranges from 0.1 to 1  $\mu\text{m}$ , while the authors of [16] used single crystals ranging from 150  $\mu\text{m}$  to 3 mm in size. The slow kinetics of decomposition may have prevented this group [16] from easily observing the transition in the large single crystals.

Another potential source of offset between the transition conditions observed in our study from the previous studies is the methods used for temperature measurement. We directly measure temperature using the thermal emission of the sample, while the previous studies indirectly calculated temperature from the amount of inserted energy by the power source [17] or through known standard calibrations [16,49]. This difference may account for some of the discrepancy between the lower-pressure decomposition temperatures in the previous studies and the higher-pressure decomposition temperatures measured here. However, the data as they currently stand can still be explained by the change in the sign of the  $\Delta V$  across the decomposition boundary from positive to negative at  $\sim 12$  GPa, as is shown in Fig. 5.

The decomposition of SiC at pressure has implications for several fields. Natural SiC (moissanite after its discovery in the Canyon Diablo meteorite by Henri Moissan [50]) is rare on Earth, but nevertheless has been found in small quantities in numerous geologic settings [2,51]. A common assumption is that SiC is stable at all pressure and temperature conditions found within the Earth's lower mantle if the local chemistry favors SiC formation [52,53]. Our findings, however, indicate that SiC has a layer of instability within the Earth's mantle stretching from  $\sim 50$  to 60 GPa along a typical Earth geotherm [54] or from  $\sim 40$  to 60 GPa along a warmer geotherm [55]. This corresponds to a layer stretching from between  $\sim 1250$  to  $\sim 1500$  km deep along the typical geotherm or from  $\sim 1000$  to 1500 km deep along the warmer geotherm where any existing

SiC would decompose to Si+C. Our work indicates that the SiC forming on Earth must originate from shallower depths, as it would not be preserved on a journey up through this layer from the deep mantle. An exception is within subducting slabs, where the temperature conditions would remain low enough to keep B3 SiC stable at pressures below the B3 to B1 transition [56]. Interestingly, many natural SiC grains contain Si inclusions [57]. We offer a possible additional interpretation of such Si inclusions as being relics from previous SiC decomposition.

Beyond the Earth, the decomposition of SiC is also important to consider for exoplanet interiors, particularly in carbon-rich solar systems. Planets with interior temperatures of over 2000 K at pressures less than 60 GPa will decompose to B3 SiC. If SiC makes up a significant fraction of a planet then the presence of C and Si rather than SiC may impact the dynamics and interior structure of such a planet.

Decomposition at high temperature is a phenomenon found in many semiconductors besides SiC although pressure effects on their decomposition are not yet well understood (i.e., [58–61]). If we consider the  $\Delta V$  of decomposition for other semiconductors we find that those containing elements heavier than carbon (such as nitrogen) are much less likely to enter a regime where the volume change across the decomposition reaction is negative, due to the larger volume of the components [62]. This may mean that the Clapeyron slope for decomposition remains positive for nitrogen-bearing semiconductors unlike the negative slope that we observe for SiC. Further investigation is necessary at high P-T conditions, however, to further our understanding of decomposition in semiconductors.

## V. CONCLUSIONS

Through a combination of *in situ* and *ex situ* measurements, we determine the temperature of the onset of decomposition in SiC at high pressures. We find that low-pressure B3 SiC decomposes at temperatures  $\sim 500$  K lower compared to ambient, possibly due to the transition of Si I to the high-density Si II structure. We find that B1 SiC does not decompose at the temperatures considered (up to  $\sim 3200$  K at 81 GPa). We present a phase diagram for SiC decomposition at high P-T and reconcile the conflicting findings of previous studies. From our measurements we infer that the shape of the phase boundary is heavily influenced by the numerous phases of carbon and silicon and their respective phase diagrams and equations of state, in addition to the high-pressure phase transition from the B3 to the B1 structure in SiC. We find that if SiC decomposition continues to occur beyond the B3 $\rightarrow$ B1 phase transition, it will require temperatures in excess of 3200 K at  $\sim 80$  GPa, but at pressures greater than  $\sim 170$  GPa, decomposition may occur at lower temperatures again following a negative phase boundary.

## ACKNOWLEDGMENTS

We acknowledge support from the Carnegie DOE Alliance Center (CDAC). We thank J. Deng for helpful discussions, J. Girard for technical assistance, Z. Jiang and J. Eckert for SEM and EPMA assistance, and Z. Liu for assistance in VIS/IR measurements. We also thank Yue Meng and

Ross Hrubik for assistance at the HPCAT IDB beamline as well as Sergey Tkachev for gas loading with the system at GSECARS. This work was performed at HPCAT (Sector 16), (APS), Argonne National Laboratory, which is supported by DOE-NNSA under Award No. DE-NA0001974 and DOE-BES under Award No. DE-FG02-99ER45775, with partial instrumentation funding by NSF. Use of the gas loading system was supported by COMPRES under NSF Cooperative Agreements EAR 11-57758, EAR 1606856 and by GSECARS through NSF Grant No. EAR-1128799 and DOE Grant No. DE-FG02-94ER14466. This research used resources of the

APS, a DOE Office of Science User Facility operated for the DOE Office of Science by Argonne National Laboratory under Contract No. DE-AC02-06CH11357. This research used resources of the Center for Functional Nanomaterials and the National Synchrotron Light Source II, which are US DOE Office of Science Facilities, at Brookhaven National Laboratory under Contract No. DE-SC0012704. The Infrared Laboratory is supported by COMPRES, under NSF Cooperative Agreement EAR 1606856 and the DOE/National Nuclear Security Administration under Grant No. DE-NA-0002006, CDAC.

- 
- [1] G. L. Harris, *Properties of Silicon Carbide* (IET, London, 1995), p. 13.
- [2] V. Lyakhovich, *Int. Geol. Rev.* **22**, 961 (1980).
- [3] A. Speck, M. Barlow, and C. Skinner, *Mon. Not. R. Astron. Soc.* **288**, 431 (1997).
- [4] S. Amari, R. S. Lewis, and E. Anders, *Geochim. Cosmochim. Acta* **58**, 459 (1994).
- [5] M. Mayor and D. Queloz, *Nature* **378**, 355 (1995).
- [6] M. J. Kuchner and S. Seager, [arXiv:astro-ph/0504214](https://arxiv.org/abs/astro-ph/0504214).
- [7] N. Madhusudhan, K. K. M. Lee, and O. Mousis, *Astrophys. J. Lett.* **759**, L40 (2012).
- [8] S. Bhaumik, *Met. Mater. Process.* **12**, 215 (2000).
- [9] S. Bhaumik, C. Divakar, M. Mohan, and A. Singh, *Rev. Sci. Instrum.* **67**, 3679 (1996).
- [10] K. Daviau and K. K. M. Lee, *Phys. Rev. B* **95**, 134108 (2017).
- [11] R. Dolloff, Research study to determine the phase equilibrium relations of selected metal carbides at high temperatures, Report No. WADD-TR-60-143, 1960.
- [12] E. Ekimov, R. Sadykov, S. Gierlotka, A. Presz, E. Tatyani, V. Slesarev, and N. Kuzin, *Instrum. Exp. Tech.* **47**, 276 (2004).
- [13] W. Gust, A. Holt, and E. Royce, *J. Appl. Phys.* **44**, 550 (1973).
- [14] H. T. Hall, Final report US Army Office of Ordnance Research, contract No. DA 04 495 ORD 792, Brigham Young University, 36 (1956).
- [15] T. Sekine and T. Kobayashi, *Phys. Rev. B* **55**, 8034 (1997).
- [16] P. S. Sokolov, V. A. Mukhanov, T. Chauveau, and V. L. Solozhenko, *J. Superhard Mater.* **34**, 339 (2012).
- [17] M. Togaya and S. Sugiyama, *Rev. High Pressure Sci. Technol.* **7**, 1037 (1998).
- [18] Y. Wang, Z. T. Liu, S. V. Khare, S. A. Collins, J. Zhang, L. Wang, and Y. Zhao, *Appl. Phys. Lett.* **108**, 061906 (2016).
- [19] M. Yoshida, A. Onodera, M. Ueno, K. Takemura, and O. Shimomura, *Phys. Rev. B* **48**, 10587(R) (1993).
- [20] K. K. Zhuravlev, A. F. Goncharov, S. N. Tkachev, P. Dera, and V. B. Prakapenka, *J. Appl. Phys.* **113**, 113503 (2013).
- [21] C. Nisr, Y. Meng, A. MacDowell, J. Yan, V. Prakapenka, and S. H. Shim, *J. Geophys. Res.: Planets* **122**, 124 (2017).
- [22] J. Gröbner, H. L. Lukas, and F. Aldinger, *CALPHAD* **20**, 247 (1996).
- [23] P. Franke, D. Neuschütz, and Scientific Group Thermodata Europe (SGTE), *The Landolt-Börnstein Database* (Springer Materials, Berlin, 2004).
- [24] Z. Du, G. Amulele, L. R. Benedetti, and K. K. M. Lee, *Rev. Sci. Instrum.* **84**, 075111 (2013).
- [25] Z. Du, T. Gu, V. Dobrosavljevic, S. T. Weir, S. Falabella, and K. K. M. Lee, *Rev. Sci. Instrum.* **86**, 095103 (2015).
- [26] S. Arveson, B. Kiefer, Z. Liu, and K. K. M. Lee (unpublished).
- [27] Y. Akahama and H. Kawamura, *J. Appl. Phys.* **96**, 3748 (2004).
- [28] Y. Fei, A. Ricolleau, M. Frank, K. Mibe, G. Shen, and V. Prakapenka, *Proc. Natl. Acad. Sci. USA* **104**, 9182 (2007).
- [29] See Supplemental Material at <http://link.aps.org/supplemental/10.1103/PhysRevB.96.174102> for details of temperature correction modeling, additional XRD information, EBSD measurements, and analysis techniques.
- [30] Y. Meng, G. Shen, and H. Mao, *J. Phys.: Condens. Matter* **18**, S1097 (2006).
- [31] Z. Du and K. K. M. Lee, *Geophys. Res. Lett.* **41**, 8061 (2014).
- [32] J. Deng, Z. Du, L. R. Benedetti, and K. K. M. Lee, *J. Appl. Phys.* **121**, 025901 (2017).
- [33] A. Kubo, Y. Wang, C. E. Runge, T. Uchida, B. Kiefer, N. Nishiyama, and T. S. Duffy, *J. Phys. Chem. Solids* **69**, 2255 (2008).
- [34] F. Bundy, *J. Chem. Phys.* **41**, 3809 (1964).
- [35] A. Jayaraman, W. Klement, Jr., and G. Kennedy, *Phys. Rev.* **130**, 540 (1963).
- [36] S. K. Deb, M. W. M. Somayazulu, and P. F. McMillan, *Nature* **414**, 528 (2001).
- [37] B. Haberl, M. Guthrie, D. Sprouster, J. Williams, and J. Bradby, *J. Appl. Crystallogr.* **46**, 758 (2013).
- [38] T. Gu, M. Li, C. McCammon, and K. K. M. Lee, *Nat. Geosci.* **9**, 723 (2016).
- [39] A. J. Campbell, *Rev. Sci. Instrum.* **79**, 015108 (2008).
- [40] R. A. Fischer and A. J. Campbell, *Am. Mineral.* **95**, 1473 (2010).
- [41] Z. Cambaz, G. Yushin, Y. Gogotsi, K. Vyshnyakova, and L. Pereseltseva, *J. Am. Ceram. Soc.* **89**, 509 (2006).
- [42] Y. Kim, A. Zangvil, J. S. Goela, and R. L. Taylor, *J. Am. Ceram. Soc.* **78**, 1571 (1995).
- [43] F. Bundy, *J. Chem. Phys.* **38**, 631 (1963).
- [44] S. J. Duclos, Y. K. Vohra, and A. L. Ruoff, *Phys. Rev. B* **41**, 12021 (1990).
- [45] J. Hu and I. Spain, *Solid State Commun.* **51**, 263 (1984).
- [46] NIST-JANAF Thermochemical Tables, available at <http://kinetics.nist.gov/janaf/>
- [47] Y. Wang, J. E. Panzik, B. Kiefer, and K. K. M. Lee, *Sci. Rep.* **2**, 520 (2012).
- [48] J. M. Montgomery, B. Kiefer, and K. K. M. Lee, *J. Appl. Phys.* **110**, 043725 (2011).
- [49] V. A. Mukhanov, P. S. Sokolov, and V. L. Solozhenko, *J. Superhard Mater.* **34**, 211 (2012).

- [50] H. Moissan, C. R. Acad. Sci., Paris **139**, 773 (1904).
- [51] R. B. Trumbull, J.-S. Yang, P. T. Robinson, S. Di Piero, T. Vennemann, and M. Wiedenbeck, *Lithos* **113**, 612 (2009).
- [52] G. C. Ulmer, D. E. Grandstaff, E. Woermann, M. Göbbels, M. Schönitz, and A. B. Woodland, *Neues Jahrb. Mineral., Abh.* **172**, 279 (1998).
- [53] E. Mathez, R. Fogel, I. Hutcheon, and V. Marshintsev, *Geochim. Cosmochim. Acta* **59**, 781 (1995).
- [54] J. Brown and T. Shankland, *Geophys. J. Int.* **66**, 579 (1981).
- [55] O. L. Anderson, *Evolution of the Earth* (American Geophysical Union, 2013), pp. 19.
- [56] E. Ohtani, *Chem. Geol.* **418**, 6 (2015).
- [57] L. Dobrzhinetskaya, P. Mukhin, Q. Wang, R. Wirth, E. O'Bannon, W. Zhao, L. Eppelbaum, and T. Sokhonchuk, *Lithos* (2017), doi: [10.1016/j.lithos.2017.04.001](https://doi.org/10.1016/j.lithos.2017.04.001).
- [58] S. Porowski, B. Sadovyi, S. Gierlotka, S. Rzoska, I. Grzegory, I. Petrusha, V. Turkevich, and D. Stratiichuk, *J. Phys. Chem. Solids* **85**, 138 (2015).
- [59] H.-F. Lee, K. Esfarjani, Z. Dong, G. Xiong, A. A. Pelegri, and S. D. Tse, *ACS Nano* **10**, 10563 (2016).
- [60] L. H. Dreger, V. Dadape, and J. L. Margrave, *J. Phys. Chem.* **66**, 1556 (1962).
- [61] A. Edwards, T. Slykhouse, and H. Drickamer, *J. Phys. Chem. Solids* **11**, 140 (1959).
- [62] M. Eremets, A. Gavriiliuk, N. Serebryanaya, I. Trojan, D. Dzivenko, R. Boehler, H. Mao, and R. Hemley, *J. Chem. Phys.* **121**, 11296 (2004).
- [63] W. Lee and X. Yao, *Comput. Mater. Sci.* **106**, 76 (2015).
- [64] I. V. Aleksandrov, A. F. Goncharov, A. N. Zisman, and S. M. Stishov, *Sov. Phys. JETP* **66**, 384 (1987).

## 1 **Supplemental Material**

### 2 **SiC Absorption Measurements and Temperature Correction Forward Modeling**

3

4 We consider the possibility that our measured temperatures are offset due to wavelength  
5 dependent absorption of the SiC samples [1]. We measure the absorption spectra of several SiC  
6 samples at a range of pressures and at different stages of heating and use the results to run a  
7 forward model estimating the temperature offset caused by the absorption of SiC. We find that  
8 the offset is typically small enough to be within our error bars but that the absorption of SiC does  
9 alias the temperature measured across the sample.

10 We conduct our own absorption measurements across the visible wavelengths as few  
11 previous studies have considered SiC absorption in the pressure and temperature range relevant  
12 to our experiments. Infrared measurements have been carried out in detail to better understand  
13 the spectra of carbon stars [2], although they primarily focus on longer wavelengths than our  
14 measurements are concerned with. Temperature has been observed to change the absorption  
15 properties of SiC thin films as the transmittance of SiC was measured to be slightly higher at  
16 1200 K as compared to 1050 K [3]. Pressure effects on the infrared absorption of SiC have been  
17 explored previously by [4, 5] up to 43 GPa finding a shift in the transverse and longitudinal  
18 phonon vibrational frequencies. Our measurements consider absorption over the shorter, visible  
19 wavelengths as compared to previous studies. We also aim to constrain the absorption changes  
20 that remain after SiC has been heated to high temperatures.

21 We measured the absorption of SiC samples at various stages of heating at the offline  
22 VIS/IR absorption lab at the National Synchrotron Light Source (NSLS) II at Brookhaven  
23 National Lab (BNL). Thin SiC foils were loaded with KCl into pre-indented Re gaskets and  
24 brought up to a range of pressures (13, 35 and 52 GPa). Each sample was laser heated at Yale  
25 University using the four-color system until the visible absorption changes were achieved. The  
26 pressurized and heated samples were then taken to BNL where we measured sample absorption  
27 across a wide range of wavelengths, covering the visible to the infrared, and across the heated  
28 and unheated portions of each sample (Fig. S1). Due to the very small size of the heated, opaque  
29 region ( $< 10 \mu\text{m}$ ) we were unable to measure a reliable absorption value for this feature.  
30 Measurements of this region consistently showed absorption spectra similar to the translucent  
31 region or in between that of the translucent and unheated regions due to our sampling the

32 translucent surroundings during measurements. After measuring the sample absorption, we  
33 cross-sectioned one of the samples (13 GPa) to determine the typical sample thickness so as to  
34 calculate the absorption coefficient. As expected, we see a smaller absorbance value in the  
35 heated translucent region, though the trend with wavelength remains nearly parallel between the  
36 heated and unheated locations on the sample.

37         Based on the forward modeling done in [1] we calculate the expected temperature offset  
38 from the ratio of optical thicknesses ( $\tau_\lambda$ ) of SiC (Figure S2), where  $\tau_\lambda = \int_0^d k_\lambda dz$ , where  $k_\lambda$  is  
39 the absorption coefficient at wavelength  $\lambda$  of the low (580 nm) and high (905 nm) wavelengths  
40 and sample thickness  $d$ . We compare the expected temperature offset for a measured  
41 temperature of 2000 K and find that all of our optical thickness measurements lie between the  
42 curves representing a minimal temperature correction of 0 K and 200 K at a temperature of 2000  
43 K. As we ascribe a temperature uncertainty of  $\pm 8\%$  due to the optics in our heating system [6],  
44 these offset estimates are typically within our error bars.

45         Using the forward radiative transfer model [1], we calculate how the sample geometry  
46 will impact our temperature maps throughout heating. We consider two separate cases; first we  
47 consider a scenario early on in heating in which SiC has become translucent but not opaque. In  
48 this three-layer model we consider a layer of transparent thermal insulation (such as KCl or Ne)  
49 and a layer of translucent SiC across the heated area. We estimate the absorbance of this layer to  
50 be that which we measured across the heated, translucent samples at BNL. The final layer in the  
51 model is composed of unheated SiC, which we prescribe the measured absorbance of the  
52 unheated sample. We find that a sample with this geometry and these absorption values will  
53 result in a temperature correction of only  $\sim 40$  K across the hottest region. We find that the  
54 profile of the hotspot is fairly typical with the hottest portion of the sample in the center (Fig. S3)

55         We also consider a scenario during the later stages of heating in which we have formed  
56 both a translucent region as well as a more opaque region in the center of the hot spot. For this  
57 model we introduce a thin layer of absorbing material in the center of the translucent layer so  
58 that we are now considering a five-layer model (transparent insulation – translucent heated –  
59 opaque heated – translucent heated – unheated). As we could not get a reliable measurement of  
60 the absorption of the small opaque heated region, we use the absorbance value for the unheated  
61 region multiplied by a scalar (factor of 1-5) to increase the absorption. We run the model for  
62 several different scalars and do not find that either the magnitude of the temperature correction

63 or the shape of the temperature profile dramatically changes. Setting the absorption of the dark  
64 heated center equal to that of unheated SiC (scalar of 1) results in the measured temperature in  
65 the center being slightly higher than the actual temperature. A higher absorption (scalar of 5)  
66 results in the measured temperature being slightly lower than the actual temperature. The offset  
67 between the apparent and corrected temperatures is no more than  $\sim 40$  K, even when the dark  
68 center has an absorption 5 times that of unheated SiC. We find that our measured temperatures  
69 are very close to the actual temperature, but that the center of the hot spot appears to be colder  
70 than the edges when we introduce the opaque heated region (Fig. S4). This corresponds well to  
71 features that we see in the measurements. We conclude two things from our models 1) our actual  
72 temperatures are close to the measured temperatures and therefore fall in the 8% error range we  
73 typically ascribe to our measurements and 2) the appearance of the opaque heated layer  
74 corresponds to an apparent temperature map with a cooler center and hotter edge. We observe  
75 this feature in our temperature maps, finding that the model is consistent with our experiments.  
76 Based on both the model and confirmed by optical images of samples throughout heating, we  
77 identify the appearance of an absorbing layer through the unique, but artificial, features in the  
78 temperature map brought about by the high absorption layer.

79

## 80 **X-Ray Diffraction Measurements**

81 We note that we also see the emergence of 6H-SiC diffraction in one self-insulated  
82 sample at  $\sim 17$  GPa. Although we do observe SiC decomposition in this experiment, we have not  
83 included the measurement in our phase boundary, as Ne was not present in the sample loading.  
84 The absence of Ne not only makes pressure determination difficult but also likely resulted in  
85 large pressure and temperature gradients. Possibly due to these gradients, we see 6H-SiC  
86 reflections appear at  $\sim 2400$  K after diamond had been observed at a lower temperature of  $\sim 1900$   
87 K. 6H-SiC has previously been identified as the high temperature polytype [7] although  
88 additional measurements on SiC decomposition indicated that the cubic phase would be stable  
89 above 5 GPa [8]. Our measurements indicate that 6H may be stable at higher pressures, although  
90 the gradients in the experiment make it impossible to determine the temperature range of 6H  
91 stability from this experiment.

92 In one experiment conducted at HPCAT-IDB, we observed diamond formation in a  
93 sample heated at 65 GPa in which B3 SiC transitioned to B1 SiC [9]. In this heating run, the

94 transition from B3 to B1 SiC began at 1760 K, with B1 peaks intensifying as heating continued.  
95 The B3 reflections never disappeared, however, and diamond reflections appeared later in the  
96 heating. We interpret the appearance of diamond to be due to the temperature gradients along  
97 the x-ray path. As we still observe both B1 and B3 SiC in the diffraction, we expect that the x-  
98 rays are sampling both hot and cold material. We hypothesize that diamond formation occurred  
99 in the transition between the hot and cold regions, where SiC was too cold to transition from B3  
100 to B1 but hot enough for the B3 SiC to decompose. This also points to the different kinetics on  
101 the transition between B3→B1 and SiC decomposition, suggesting that near the B3→B1  
102 transition, the kinetics of the B3→B1 transition are quicker than the kinetics of decomposition.  
103 Due to the difficulty in measuring the temperature of the decomposition in this situation, we have  
104 not included the data point in this study.

105

## 106 **Raman Spectroscopy**

107 The presence of carbon was observed by Raman spectroscopy at room temperature and  
108 unloaded samples after heating through the identification of the D and G bands as previously  
109 seen in carbide-derived carbons (CDCs) [10-12] (Main text, Fig 4). We see these Raman bands  
110 only in the region surrounding the hottest spot and the hot spot itself. The G band in our  
111 measurements typically lies around  $1585\text{ cm}^{-1}$ , shifted to lower wavenumbers than the expected  
112  $\sim 1600\text{ cm}^{-1}$ . This shift is likely due to the high temperature of SiC decomposition and carbon  
113 formation in our experiments [10]. At the absorbing center of the heated area we see a  
114 sharpening of the D band, potentially another sign of formation at high temperatures. Many  
115 factors may affect the location and shape of the D and G band, however, little work has been  
116 done constraining the effects of high-pressure CDC formation. We therefore use the presence of  
117 CDCs as an additional method of identifying regions of a sample that underwent decomposition  
118 when diffraction measurements are not available. The CDC Raman peaks do not give us specific  
119 structural information about the polymorph of C that was formed, however. Many high pressure  
120 polymorphs of C have been proposed [13] with the M-carbon structure observed to form  
121 sluggishly upon cold compression of graphite [14]. Samples that have been brought up to the M-  
122 carbon stability field and recovered still show D and G band signals in their Raman spectra [14].  
123 As we are also considering recovered samples, the observed D and G bands only indicate the  
124 presence of elemental carbon and not the initial structure that it formed upon SiC decomposition.

125

## 126 **Electron Backscatter Diffraction (EBSD)**

127 We perform EBSD measurements on a carbon-rich grain in the cross section of a sample  
128 heated at ~15 GPa. This sample was heated at HPCAT and is not included in the phase diagram  
129 due to a lack of Ne diffraction for pressure calibration. The EBSD confirms that the structure of  
130 the grain is that of carbon diamond, further supporting the x-ray diffraction measurements and  
131 the carbon enrichments seen by the EPMA (Fig. S5).

132 We see a more extensive volume of decomposition in the cross section in Figure S5 as  
133 compared to that in Figure 2. We see a considerable amount of grain growth across the heated  
134 region. The formation of small diamond grains occurs both on the interior and exterior of the  
135 SiC grains, while the largest diamond grain formed in what was presumably the hottest portion  
136 of the sample. The large volume of decomposition, as well as the varied locations of diamond  
137 formation, suggests that local pressure variations due to grain boundary interactions do not have  
138 a large effect on the observed decomposition transition.

139

## 140 **Analysis Equipment**

141 For clarity we have included a table (Table SI) detailing all of the equipment used during  
142 the experiments and sample analysis for this study.

143

144

## 145 **References**

146

147

- 148 1. Deng, J., et al., *The influence of wavelength-dependent absorption and temperature*  
149 *gradients on temperature determination in laser-heated diamond-anvil cells*. Journal  
150 of Applied Physics, 2017. **121**(2): p. 025901.
- 151 2. Mutschke, H., et al., *Infrared properties of SiC particles*. Astron. Astrophys, 1999. **345**:  
152 p. 187-202.
- 153 3. Sun, Y., T. Miyasato, and J.K. Wigmore, *Characterization of excess carbon in cubic SiC*  
154 *films by infrared absorption*. Journal of applied physics, 1999. **85**(6): p. 3377-3379.
- 155 4. Kobayashi, M., M. Yamanaka, and M. Shinohara, *High-Pressure Studies of Absorption*  
156 *and Luminescence Spectra in 3C-SiC*. Journal of the Physical Society of Japan, 1989.  
157 **58**(8): p. 2673-2676.
- 158 5. Liu, Z., et al., *Moissanite (SiC) as windows and anvils for high-pressure infrared*  
159 *spectroscopy*. Review of scientific instruments, 2004. **75**(11): p. 5026-5029.

- 160 6. Du, Z., et al., *Mapping temperatures and temperature gradients during flash heating in*  
161 *a diamond-anvil cell*. Review of Scientific Instruments, 2013. **84**(7): p. 075111-  
162 075111-9.
- 163 7. Sugiyama, S. and M. Togaya, *Phase Relationship between 3C - and 6H - Silicon*  
164 *Carbide at High Pressure and High Temperature*. Journal of the American Ceramic  
165 Society, 2001. **84**(12): p. 3013-3016.
- 166 8. Togaya, M. and S. Sugiyama, *Melting Behavior of  $\beta$ -SiC at High Pressure*. 高圧力の科  
167 学と技術= The Review of high pressure science and technology, 1998. **7**: p. 1037-  
168 1039.
- 169 9. Daviau, K. and K.K.M. Lee, *Zinc-blende to rocksalt transition in SiC in a laser-heated*  
170 *diamond-anvil cell*. Physical Review B, 2017. **95**(13): p. 134108.
- 171 10. Cambaz, Z., et al., *Formation of Carbide - Derived Carbon on  $\beta$  - Silicon Carbide*  
172 *Whiskers*. Journal of the American Ceramic Society, 2006. **89**(2): p. 509-514.
- 173 11. Urbonaite, S., L. Hälldahl, and G. Svensson, *Raman spectroscopy studies of carbide*  
174 *derived carbons*. Carbon, 2008. **46**(14): p. 1942-1947.
- 175 12. Büke, G.C., et al., *Effect of defects on graphitization of SiC*. Journal of Materials  
176 Research, 2013. **28**(07): p. 952-957.
- 177 13. Wang, Y. and K. Lee, *From soft to superhard: Fifty years of experiments on cold-*  
178 *compressed graphite*. Journal of Superhard Materials, 2012. **34**(6): p. 360-370.
- 179 14. Wang, Y., et al., *Crystal structure of graphite under room-temperature compression*  
180 *and decompression*. Scientific reports, 2012. **2**.
- 181 15. Akahama, Y. and H. Kawamura, *High-pressure Raman spectroscopy of diamond anvils*  
182 *to 250 GPa: Method for pressure determination in the multimegabar pressure range*.  
183 Journal of applied physics, 2004. **96**: p. 3748-3751.
- 184

## 185 Figure Captions

186

187 **Figure S1.** Absorption spectra measured across the heated translucent and unheated regions of a  
188 SiC sample at 13 GPa. The heated translucent region is less absorbing than the unheated region  
189 over both the infrared and visible wavelengths, although the shapes of the spectra are very  
190 similar. A FIB-ed cross section indicates that the sample is consistently 5  $\mu\text{m}$  thick. The four-  
191 color temperature measurement is completed over the wavenumbers 17241, 15625, 13054, and  
192 11049  $\text{cm}^{-1}$ , corresponding to wavelengths used in multi-wavelength imaging radiometry: 580,  
193 640, 766 and 905 nm.

194

195 **Figure S2.** Optical thickness calculated across the visible wavelengths used to fit for  
196 temperature. Clockwise from top left: a) unheated (solid circles) and heated translucent (open  
197 circles) regions at 13 GPa, b) unheated (solid squares) and heated translucent (open squares)  
198 regions at 35 GPa, c) unheated (solid triangles) and heated translucent (open triangles) regions at  
199 52 GPa, d) comparison of the optical thickness at the shortest and longest wavelengths and at  
200 each pressure. Due to noise in the absorption spectra of the 13 GPa sample, we extrapolate the  
201 optical thickness from the higher wavelength data to find the optical thickness at 580 nm at 13  
202 GPa. The dotted lines correspond to the magnitude and direction of an expected temperature

203 correction from [1]. All of the absorption measurements for SiC lie within the 0 K and 200 K  
204 temperature correction, with most lying closer to the 0 K correction curve.

205  
206 **Figure S3.** Forward modeling of temperature as compared to experimental results for the first  
207 stage of heating prior to formation of the absorbing central region. The model geometry is  
208 depicted on the top left and consists of a transparent pressure medium, translucent heated region,  
209 and opaque unheated material. The bottom left is a plot of the measured temperature for an  
210 actual temperature of 1550 K. We compare this to the measured emissivity and temperature  
211 maps of a heated sample on the right. The model indicates that an actual temperature of 1550 K  
212 would look like a temperature of ~1590 K. We measure a temperature of ~1590 K in the  
213 experiment, indicating that we may be ~40 K too high, well within our uncertainties.

214  
215 **Figure S4.** The same as Figure S3. but for a sample during the later stages of heating after the  
216 formation of the dark absorbing center. Here we use a five-layer model with the introduction of  
217 an absorbing region (scalar set equal to 5) in the center of the translucent heated region. We find  
218 that the temperature offset for a sample at 2000 K is small (only ~20 K) but that the introduction  
219 of the absorbing region results in an “inverse” temperature profile with the center seeming cooler  
220 than the edges. We compare this to a measured temperature and find a similar “inverse” profile.

221  
222 **Figure S5.** The FIBed cross-section of sample after heating at 15 GPa a) Region of the polished  
223 cross section across the heated area showing the large diamond grain for which EBSD was  
224 performed. The circular “bull’s eye” damage feature marks the location where the EBSD  
225 measurement was taken, b) Electron backscatter pattern raw measurement, c) Raw pattern  
226 overlaid with calculated lines for cubic diamond.

227

228

229

230

231

232

233

234

235

236

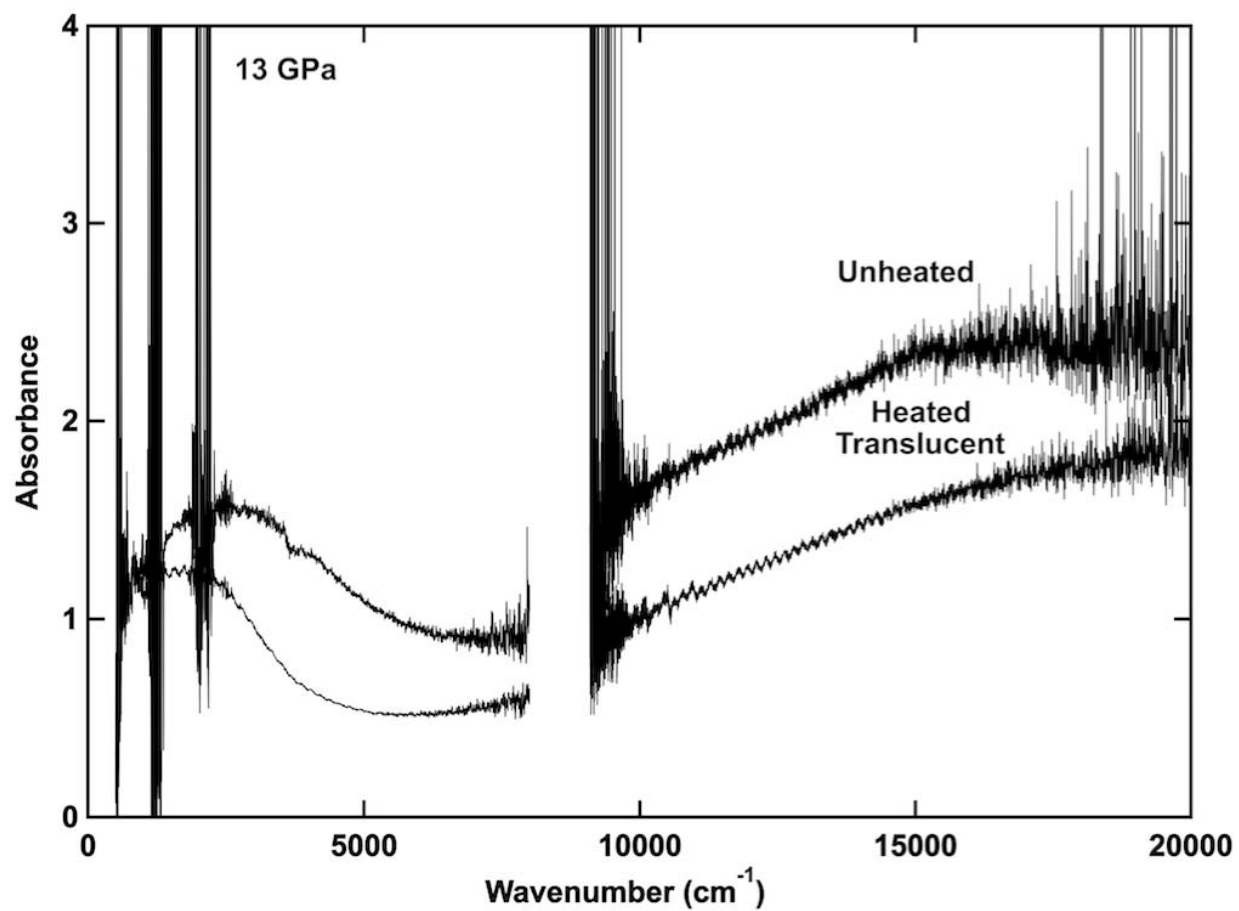
237

238

239

240

241 Figure S1.



242

243

244

245

246

247

248

249

250

251

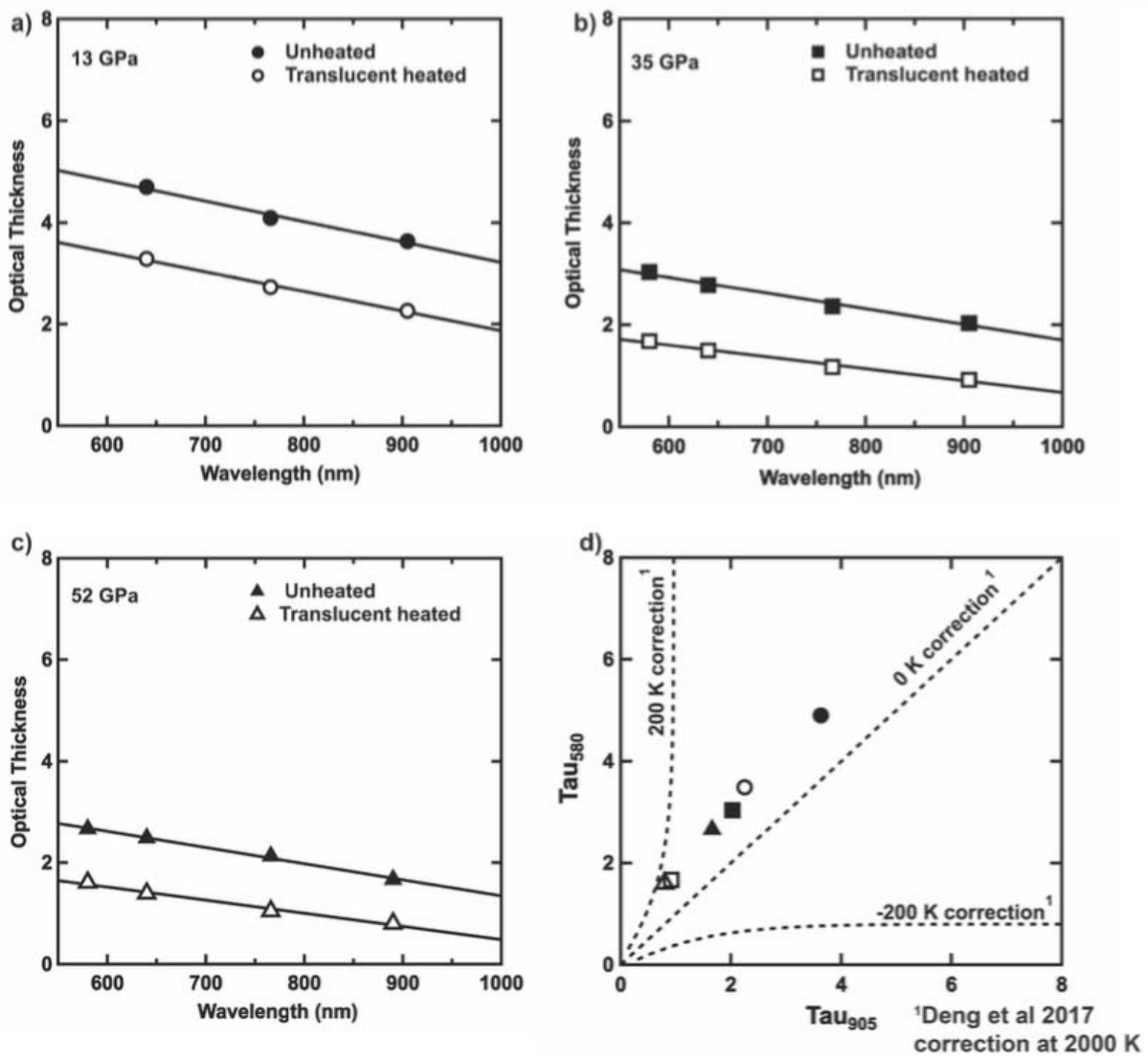
252

253

254

255

256 Figure S2.



257

258

259

260

261

262

263

264

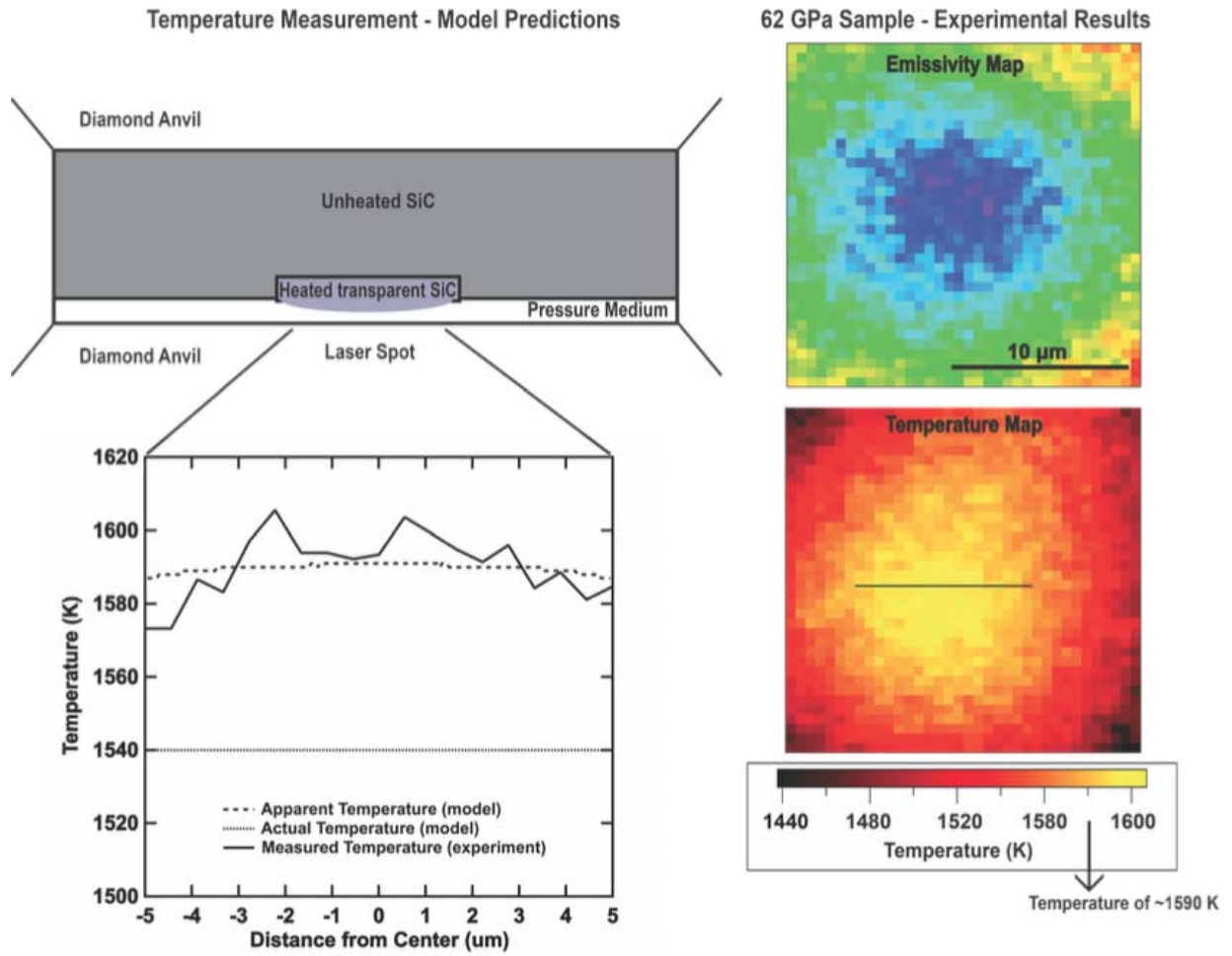
265

266

267

268 Figure S3.

### Wavelength dependent absorption in mid-temperature SiC: Models vs Experiment



269

270

271

272

273

274

275

276

277

278

279

280

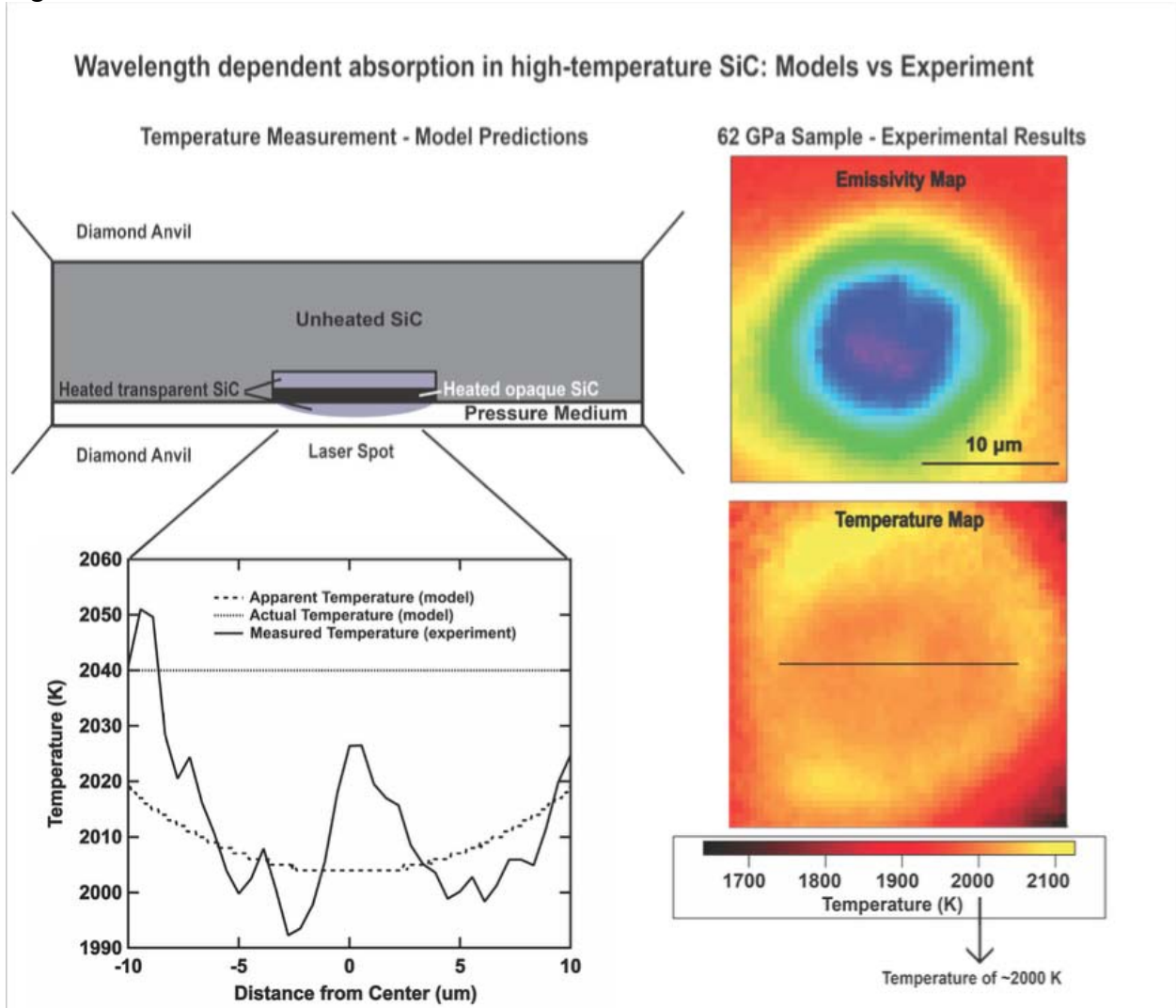
281

282

283

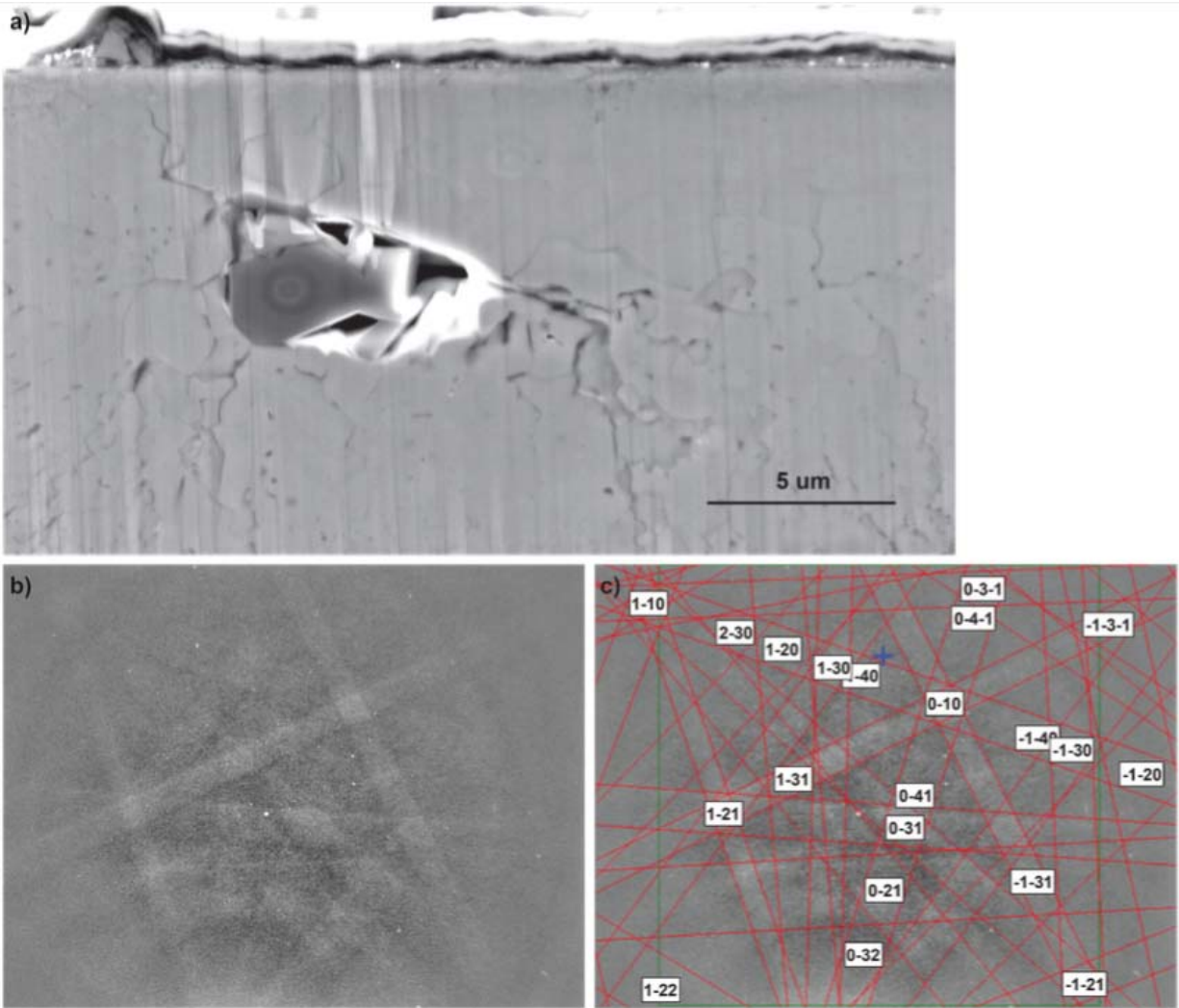
284  
285

Figure S4.



286  
287  
288  
289  
290  
291  
292  
293  
294  
295  
296  
297  
298  
299  
300  
301

302 Figure S5.  
303



304  
305  
306  
307  
308  
309  
310  
311  
312  
313  
314  
315  
316  
317  
318  
319  
320

TABLE SI. Summary of experimental and analysis equipment

Analysis Equipment Used	Type of Analysis	Further details
Raman Spectroscopy	Pressure determination (from diamond anvil [15]); structural information (of sample)	Horiba-Jobin Yvon HR-800 Raman Microscope equipped with a 50 mW green laser tuned to 532 nm with an 1800 lines/mm grating
Electrical Discharge Machine (EDM)	Remove excess gasket material to prepare sample for FIB	Hylozoic Micro-EDM for drilling gasket holes
Focused Ion Beam (FIB)	Cutting cross sections of post heated samples	FEI Helios Nanolab dual-beam system capable of simultaneous focused ion beam milling ( $\text{Ga}^+$ ) and SEM imaging
Scanning Electron Microscope (SEM)	Optical information/image collection of cross sectioned samples	XL-30 Environmental Scanning Electron Microscope (ESEM) with a field emission electron gun (FEG) and equipped various detectors such as an EDS system (PGT) and an EBSD system (HKL Technology).
Electron Backscatter Diffraction (EBSD)	Structural information	Detector on the XL-30 SEM used (see above)
Electron Probe Microanalysis (EPMA)	Elemental composition, both qualitative maps and quantitative spot measurements	JEOL JXA-8530F (FEG) "Hyperprobe" - electron probe microanalyzer (electron microprobe analyzer, or EMPA), includes five wavelength-dispersive spectrometers (WDS) and a light-element-capable energy-dispersive spectrometer (EDS) with Windows-XP processing software.